Data Paper

The Katwijk beach planetary rover dataset

**Robert A Hewitt[1,2], Evangelos Boukas[1,3], Martin Azkarate[1],
Marco Pagnamenta[1], Joshua A Marshall[2], Antonios Gasteratos[4]
and Gianfranco Visentin[1]**

Abstract

This paper describes a dataset collected along a 1 km section of beach near Katwijk, The Netherlands, which was populated with a collection of artificial rocks of varying sizes to emulate known rock size densities at current and potential Mars landing sites. First, a fixed-wing unmanned aerial vehicle collected georeferenced images of the entire area. Then, the beach was traversed by a rocker-bogie-style rover equipped with a suite of sensors that are envisioned for use in future planetary rover missions. These sensors, configured so as to emulate the ExoMars rover, include stereo cameras, and time-of-flight and scanning light-detection-and-ranging sensors. This dataset will be of interest to researchers developing localization and mapping algorithms for vehicles traveling over natural and unstructured terrain in environments that do not have access to the global navigation satellite system, and where only previously taken satellite or aerial imagery is available.

1. Introduction

This paper describes a large dataset collected on a section of beach near Katwijk, The Netherlands. The beach was chosen as a Mars analog since it is a natural, unstructured, and sandy terrain that is also located near the European Space and Technology Research Center where the heavy-duty planetary rover (HDPR) research platform used in this paper was developed (shown in Fig. 1). The development of HDPR and the creation of this dataset has served to build up and evaluate capabilities for future field experiments at analog sites with this platform, similar in scope to Bakambu et al. (2016), in advance of the ExoMars rover mission that is currently scheduled for 2020.

This dataset is intended for research on localization and mapping in global navigation satellite system (GNSS)-denied environments, especially with respect to planetary rovers or similar operational scenarios. In the past, field campaigns have been performed to support this type of research (Bakambu et al., 2014; Wettergreen et al., 2005; Woods et al., 2014a,b) but the datasets generated were not made with the intention of being broadly reusable. Other datasets have presented longer traverses in more Mars-like terrain (Furgale et al., 2012). In contrast, this dataset aims to include new types of measurements that will be useful

for research on a platform that is more representative of planetary rovers. Its distinguishing features are as follows.

1. The HDPR has an instrumented rocker-bogie suspension system, similar to the chassis designs of all current Mars rovers, including NASA's Mars Science Laboratory.
2. A Sensefly eBee unmanned aerial vehicle (UAV) was flown before each traverse to capture georeferenced images with a resolution of approximately 2 cm. Digital elevation maps were also created with an accuracy in the elevation direction of approximately 20 cm. This was done to simulate images taken by the HiRise camera on-board the Mars Reconnaissance Orbiter (MRO).

[1]European Space Agency (Section of Robotics and Automation TEC-MMA), The Netherlands
[2]Queen's University (Mining Systems Laboratory), Canada
[3]Aalborg University Copenhagen (Robotics Vision and Machine Intelligence Laboratory), Denmark
[4]Democritus University of Thrace (Laboratory of Robotics and Automation), Greece

Corresponding author:
Robert Hewitt, Mining Systems Laboratory, Queen's University, 35 5 Field Company Lane, Jackson Hall, Room 112, Kingston, Ontario, K7L 3N6, Canada.
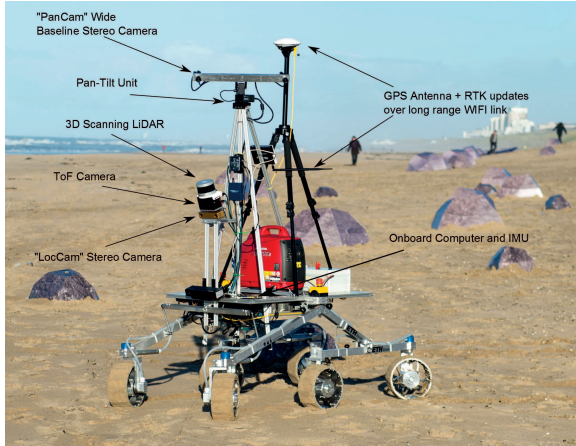Email: r.hewitt@queensu.ca

Fig. 1. Heavy-duty planetary rover (HDPR) platform used to collect data from the ground (GPS: global positioning system; RTK: real-time kinematic; IMU: inertial measurement unit).

3. Like ExoMars, HDPR includes localization and Pan-Cam stereo-benches (mounted on a pan–tilt unit). The sensor specifications and the design of the custom stereo-bench were chosen to closely approximate the ExoMars camera systems, using commercially available hardware (Coates et al., 2015).

4. Two active sensors—a Velodyne VLP-16 three-dimensional (3D) scanning light detection and ranging (LiDAR) and an outdoor-rated MESA SwissRanger 4500 time-of-flight (ToF) camera—were positioned above the localization cameras. To the authors' knowledge, this is the first published dataset that includes long traverses with an outdoor ToF camera.

5. Artificial rocks were made in three sizes, to approximate known rock size densities at current and potential future Mars landing sites (Golombek et al., 2012). These rocks are visible in both the HDPR and eBee images. The ground-truth position of these rocks was obtained from the georeferenced UAV images. Dimensions of the three rock types are also included.

The dataset is partitioned into two parts: (1) rover traverse data with two sets of stereo images, pan and tilt orientations from a pan–tilt unit, scanning LiDAR and ToF measurements, inertial measurement unit (IMU) data, real-time kinematic (RTK) global positioning system (GPS) position; and (2) fixed-wing UAV eBee georeferenced images and digital elevation maps (DEMs) taken before each traverse. The full dataset is available for download at https://robotics.estec.esa.int/datasets/katwijk-beach-11-2015.html.

This webpage also includes descriptions of all available data and file formats and provides some tools to make use of the data.

The remainder of this paper is organized as follows. Section 2 introduces the rover traverse data, including frame conventions and calibration values. Section 3 describes the

eBee georeferenced images and DEMs and Section 4 discusses ways this dataset can be used and some lessons learned during the creation of this dataset.

2. HDPR traverse data

Stereo imagery, pan–tilt encoders, active sensor (ToF and scanning LiDAR), IMU, wheel encoder, and RTK GPS measurements were all taken using the HDPR research platform described first in Boukas et al. (2016). GPS measurements were recorded in both the World Geodetic System 84 (WGS 84) and Universal Transverse Mercator Zone 31 North (UTM 31 N) reference frames. Details about these data are presented in Table 1. A single on-board computer logged and timestamped all sensor data as it arrived, including GPS data (which includes a GPS-derived timestamp). All sensors operate independently (i.e. the sensors were not time-synchronized). However, stereo camera image pairs (or triples in the case of the Velodyne VLP-16) were acquired simultaneously.

Three traverses took place on 26 November 2015 and are shown in Figure 2. The density of rocks greater than 1.2 m for the first two traverses was chosen to match an area of *Medium-Low* to *Medium-High* density of rocks north-west of the Bagnold Dunes in Gale Crater on Mars described in Golombek et al. (2012), where the Mars Science Laboratory landed in 2012 and has since spent its time traversing. At these locations, rocks greater than 1.2 m in diameter have a density of $0.0031/m^2$ to $0.0054/m^2$. To approximate this, 100 rocks of 1.326 m diameter and 12 rocks of 1.897 m diameter were produced for a rock density of $0.0045/m^2$ over an area of 1000 m $\times$ 25 m. While rocks less than 1.2 m are not reliably detected with algorithms that use HiRise orbital imagery (Golombek et al., 2012), an additional 100 rocks of 0.737 m size were added to provide more features for rover-based localization algorithms. The three sizes of rocks produced are shown in Fig. 3. The rocks are simple geometrical shapes with flat surfaces, a design that was necessary to produce them from flat pieces of cardboard with minimal construction effort. The flat surfaces were particularly useful for evaluating algorithms that estimate surface normals such as the one presented in Hewitt and Marshall (2015), where the 3D models provide a ground-truth shape.

The first traverse, approximately 1.026 km in length, took place between 12:53 and 13:33 where the rover traversed through a "rock field" made up of the 212 artificial rocks at a median speed of 0.5077 m/s (speed profiles over all traverses are shown in Figure 4). The second traverse contains data from the return journey to the starting location over a 0.797 km traverse and took place from 13:39 to 14:06 at a median speed of 0.5057 m/s. Short stops occurred twice in the first traverse, and once in the second traverse due to a loss of GPS RTK measurements, but resumed shortly after these measurements returned. Both traverses are shown in Figure 2(a).
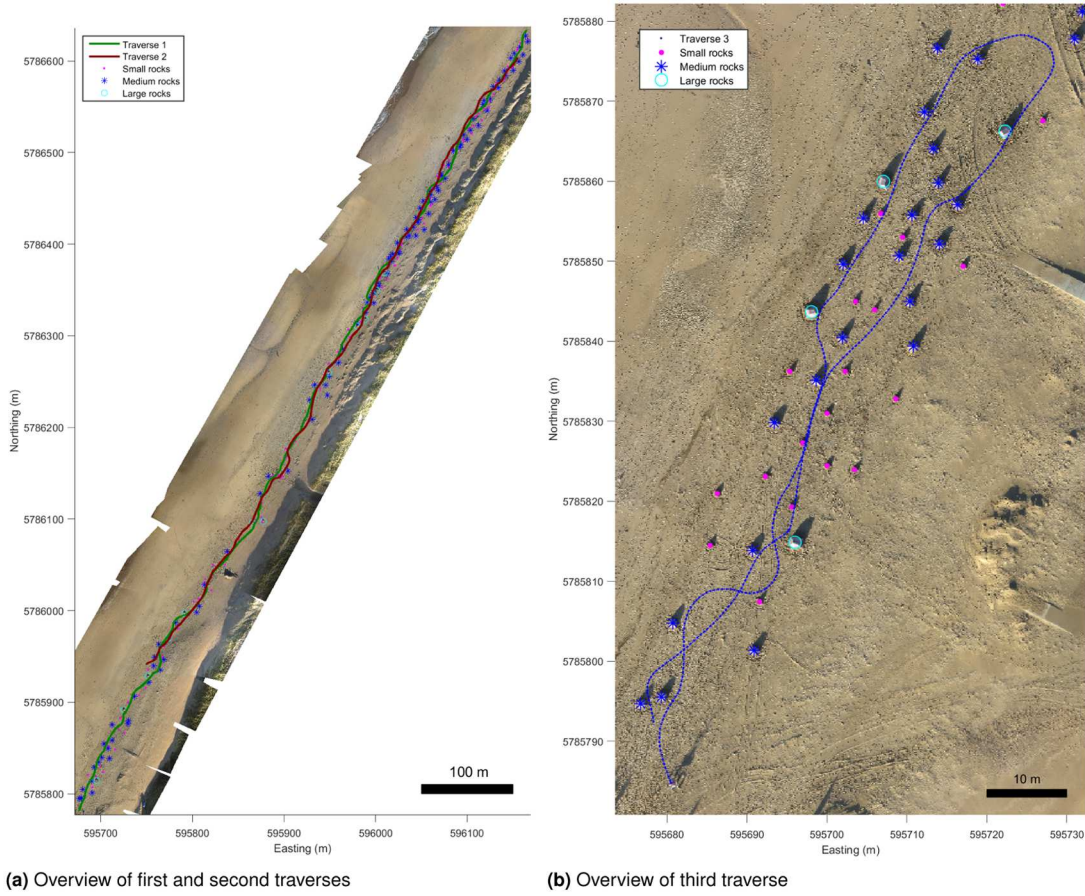
(a) Overview of first and second traverses

(b) Overview of third traverse

Fig. 2. UTM 31 N projection of all traverses.

Table 1. Overview of the sensors and data collected over the traverse.

| Sensor	Description	Data logged	Measurements	Capture rate
LocCam	PointGrey Bumblebee2 (BB2-08S2C-38) 12 cm baseline stereo camera	Color 1024 × 768 images	~20,000 pairs	3.75 Hz
PanCam	PointGrey GrassHopper2 (GS2-FW-14S5C-C) ×2 custom 50 cm baseline stereo camera	Color 1280 × 960 images	~12,000 pairs	3.75 Hz
ToF camera	MESA SwissRanger 4500	Depth and intensity 176 × 144 images	~47,000 pairs	10 Hz
3D LiDAR	Velodyne VLP-16	Range, azimuth, intensity 1808 × 16 images	~33,000 triples	10 Hz
RTK GPS	Trimble BD 970 receiver with Zephyr Model 2 antenna (rover) Trimble BX 982 Receiver with Zephyr Geodetic antenna (base station)	Latitude, longitude and altitude expressed on WGS 84 ellipsoid	1790 sets	0.3 Hz
IMU	Sensonor STIM 300 IMU	Pitch, roll, three-axis acceleration and angular velocity	~670,000 sets	125 Hz
Wheel encoders	Maxon motor encoders	Six wheel rotation rate	~67,000 sets	13 Hz
Pan–tilt encoders	Directed perception PTU-D46 motor encoders	Pan, tilt	~12,000 pairs	2.25 Hz
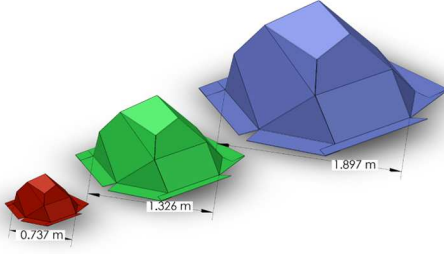
Fig. 3. The three rock models used for construction and included in this dataset.

The reason this dataset is split into two parts is due to poor lighting conditions on the return traverse, which caused blooming in some of the stereo images. These variations in lighting may be useful to some researchers who wish to test under such conditions. The third traverse is shown in Figure 2(b) and took place from 15:00 until 15:22. It was driven at a slower median speed of 0.1813 m/s for a distance of approximately 0.221 km over an area of 100 m × 25 m. In this traverse 27 artificial rocks were placed such that a *High* density of 0.011/m^2 was matched as described by Golombek et al. (2012) for rocks greater than 1.2 m in diameter along with 19 smaller rocks primarily used for rover-based imagery. This produced images with less motion blur, and more targets to track for algorithms such as visual odometry.

Two sets of stereo pairs were taken, and serve different roles which correspond to the two stereo cameras on the upcoming ExoMars rover mission. The first set was taken using a PointGrey Bumblebee2 stereo camera, mounted at the same height and angle as the ExoMars rover LocCam. Its intended primary use is for visual odometry. The second set was taken using a custom 50 cm baseline stereo camera, mounted at the same height as the ExoMars PanCam on a pan–tilt unit. This set is intended for scene reconstruction and was periodically taken at varying pan angles throughout the traverses.

For ground truth, a pair of Trimble GPS units were used for the rover's position. One was set up as a base station near the beginning of the traverse; the second was mounted on the rover. The base station provided DGPS differential GPS and RTK corrections throughout the traverse, resulting in a position estimate with an accuracy as high as 2 mm at approximately 0.3 Hz.

The terrain, multitude of sensors, and use of a representative research platform make this a unique dataset that is relevant to future planetary rover missions (Boukas et al., 2015), as well as being useful to mobile robotics researchers developing localization algorithms that do not rely on GNSS measurements and/or that must be lighting-invariant (e.g. algorithms for mining or military vehicles). In addition, the SwissRanger ToF sensor was used to collect both range and intensity images. The intensity images can be used to perform feature-tracking for visual odometry

(McManus et al., 2013) and advanced photometric techniques (Hewitt and Marshall, 2015) that are currently of interest to the European Space Agency for future missions.

2.1. Transformations and data format

HDPR and all relevant sensor frames are shown in Fig. 5 and explained in Table 2. All sensors were mounted according to a reference design, with the mounting position and rotation measured by hand with an uncertainty of a few mm (one standard deviation) and an uncertainty in rotation of approximately 1° (one standard deviation).

For consistency, we adopt the transformation representations described by Furgale et al. (2012). Thus, rotations are described by an axis angle representation, with a unit vector axis, **a**, and an angle, θ, that can be used to construct a rotation matrix

$$\mathbf{R} = \cos\theta \mathbf{1} + (1 - \cos\theta)\mathbf{a}\mathbf{a}^{\mathrm{T}} + \sin\theta \mathbf{a}^{\times} \quad (1)$$

where $(\cdot)^{\times}$ is the skew-symmetric matrix operator

$$\begin{bmatrix} a_x \\ a_y \\ a_z \end{bmatrix}^{\times} = \begin{bmatrix} 0 & -a_z & a_y \\ a_z & 0 & -a_x \\ -a_y & a_x & 0 \end{bmatrix} \quad (2)$$

A translation is expressed as $\boldsymbol{\rho}_a^{ba}$ which describes a vector from the origin of $\mathcal{F}_a$ to the origin of $\mathcal{F}_b$ (shown by the superscript) expressed in $\mathcal{F}_a$ (shown by the subscript). A 4 × 4 transformation matrix can then be formed that takes points expressed in $\mathcal{F}_b$ to $\mathcal{F}_a$:

$$\mathbf{T}_{ab} = \begin{bmatrix} \mathbf{R}_{ab} & \boldsymbol{\rho}_a^{ba} \\ \mathbf{0}^T & 1 \end{bmatrix} \quad (3)$$

The ground-truth pose of a given sensor is determined by transforming the GPS measurements and IMU orientation estimates into the sensor frame by using the provided MATLAB® tools. An overview of many inter-sensor transformations is shown in Table 3, and through successive transformations they can be used to transform any measurement to the IMU frame. For instance, a point, $\mathbf{p}_{p_r}$, expressed in the right PanCam frame would be expressed in the IMU frame by

$$\mathbf{p}_z = \mathbf{T}_{zd}\mathbf{T}_{dpc}\mathbf{T}_{pcp_r}\mathbf{p}_{p_r} \quad (4)$$

Note that the PanCam sensors are mounted on a pan–tilt unit that periodically rotated the stereo-bench during the traverse to cover a wider field of view. Therefore, the transformation that describes this sensor is dependent on the corresponding pan–tilt unit's measurements at each image's time stamp, found in the ptu.txt files shown in Table 5. The transformation from $\mathcal{F}_{\overrightarrow{pc}}$ to $\mathcal{F}_{\overrightarrow{d}}$ is computed as

$$\mathbf{T}_{dpc} = \begin{bmatrix} \mathbf{R}_{dpc} & \boldsymbol{\rho}_d^{pcd} \\ \mathbf{0}^T & 1 \end{bmatrix} \quad (5)$$

$$\mathbf{R}_{dpc} = \begin{bmatrix} s_{\theta_p} & -c_{\theta_p}s_{\theta_t} & c_{\theta_p}c_{\theta_t} \\ -c_{\theta_p} & -s_{\theta_p}s_{\theta_t} & c_{\theta_t}s_{\theta_p} \\ 0 & -c_{\theta_t} & -s_{\theta_t} \end{bmatrix} \quad (6)$$
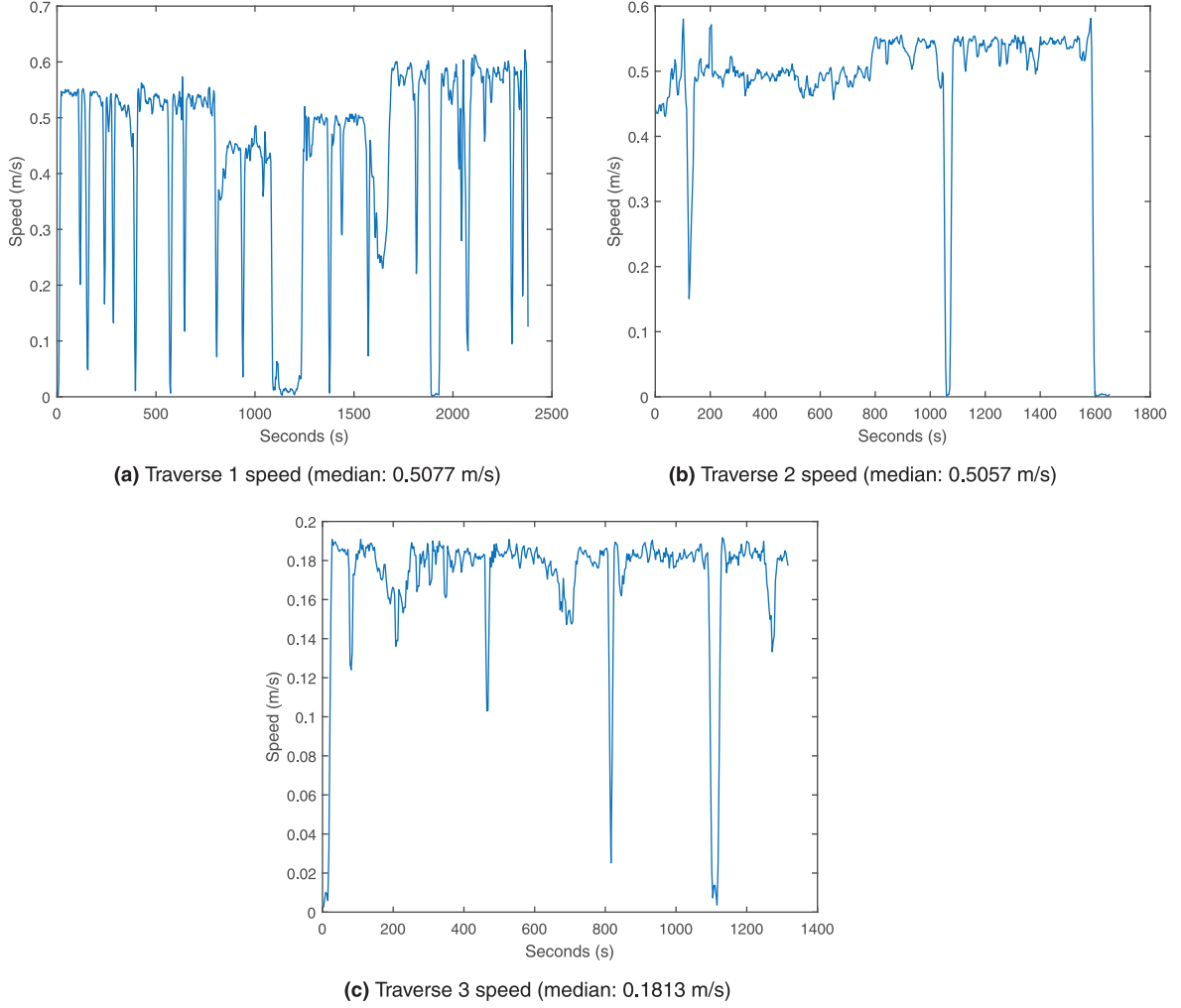
(a) Traverse 1 speed (median: 0.5077 m/s)

(b) Traverse 2 speed (median: 0.5057 m/s)

(c) Traverse 3 speed (median: 0.1813 m/s)

Fig. 4. Speed profile for all three traverses.

Table 2. Coordinate frames associated with each sensor.

Coordinate Frame		*x*-axis	*y*-axis	*z*-axis
$\underset{\rightarrow}{\mathcal{F}_t}$	Topocentric frame	East	North	Up
$\underset{\rightarrow}{\mathcal{F}_{pc}}$	Left PanCam	Horizontal pixels	Vertical pixels	Optical axis
$\underset{\rightarrow}{\mathcal{F}_{pr}}$	Right PanCam	Horizontal pixels	Vertical pixels	Optical axis
$\underset{\rightarrow}{\mathcal{F}_{lc}}$	Left LocCam	Horizontal pixels	Vertical pixels	Optical axis
$\underset{\rightarrow}{\mathcal{F}_{lr}}$	Right LocCam	Horizontal pixels	Vertical pixels	Optical axis
$\underset{\rightarrow}{\mathcal{F}_s}$	MESA SwissRanger 4500	Horizontal pixels	Vertical pixels	Optical axis
$\underset{\rightarrow}{\mathcal{F}_v}$	Velodyne VLP-16	Toward front	Toward left	Laser spin axis
$\underset{\rightarrow}{\mathcal{F}_z}$	IMU	Toward back	Toward right	Up
$\underset{\rightarrow}{\mathcal{F}_d}$	PanCam pan–tilt		Toward left	Up
$\underset{\rightarrow}{\mathcal{F}_w}$	6× wheel encoder		Toward left	
$\underset{\rightarrow}{\mathcal{F}_\alpha}$	4× steering orientation			Up
$\underset{\rightarrow}{\mathcal{F}_\psi}$	Rocker orientation		Toward left	
$\underset{\rightarrow}{\mathcal{F}_\phi}$	2× bogie orientation		Toward left	
$\underset{\rightarrow}{\mathcal{F}_g}$	GPS antenna	—	—	—

$$\boldsymbol{\rho}_d^{p_c d} = \mathbf{R}_{dp_c}[0.010, 0.250, 0.054]^{\mathrm{T}} \qquad (7)$$

where s_θ and c_θ are shorthand for $\cos\theta$ and $\sin\theta$ respectively, and θ_p and θ_t are the measured pan and tilt angles respectively.

Similarly, the transformations to each of the wheel encoder frames are dependent on the measured rocker, ψ_1, bogie, $\phi_{1,2}$, and steering, $\alpha_{1,2,5,6}$, orientations. In all cases, these orientations were measured with respect to a zero
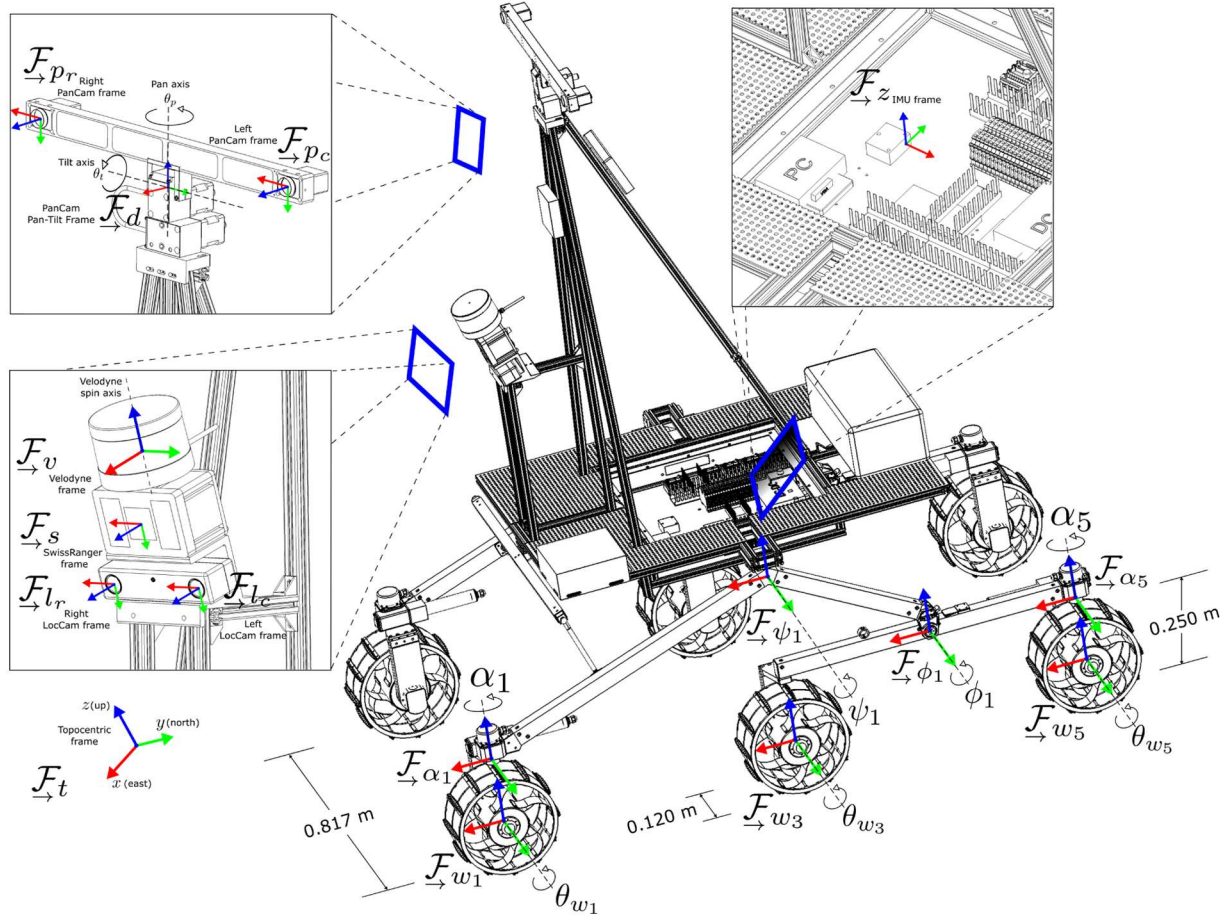
Fig. 5. HDPR and sensor coordinate frames. Not shown are the coordinate frames associated with the right side of the rover chassis: $\underset{\rightarrow}{\mathcal{F}}_{w2,4,6}, \underset{\rightarrow}{\mathcal{F}}_{\phi 2}, \underset{\rightarrow}{\mathcal{F}}_{\psi 2}, \underset{\rightarrow}{\mathcal{F}}_{\alpha 2,6}$.

Table 3. Transformations between sensor frames.

Transformation	x (m)	y (m)	z (m)	a_x	a_y	a_z	θ (rad)
$\mathbf{T}_{zl_c}$	-0.382	-0.078	0.557	-0.842	0.337	0.421	-0.589
$\mathbf{T}_{l_c l_r}$	0.120	0.000	0.000	1.000	0.000	0.000	0.000
$\mathbf{T}_{zd}$	-0.138	-0.005	1.286	0.000	0.000	1.000	3.142
$\mathbf{T}_{dp_c}$	see (5)						
$\mathbf{T}_{p_c p_r}$	0.500	0.000	0.000	1.000	0.000	0.000	0.000
$\mathbf{T}_{zs}$	-0.406	-0.018	0.627	-0.842	0.337	0.421	-0.589
$\mathbf{T}_{zv}$	-0.403	-0.018	0.717	-0.156	0.000	0.988	3.142
$\mathbf{T}_{zw\{1-6\}}$	wheelTransformation.m						
ρ_z^{gz}	0.221	-0.052	1.503	$-$	$-$	$-$	$-$

Table 4. Overview of the data collected by the eBee UAV.

Sensor	Description	Data logged	Measurements
Camera	Canon PowerShot ELPH 110 HS	Color 4608×3456 images	443 (Traverse 1+2: 154 and Traverse 3: 289)
–	Digital elevation models	UTM 31 N position, elevation	Two maps (Traverse 1+2 and Traverse 3)
–	Georeferenced images	UTM 31 N position, RGB image	Two maps (Traverse 1+2 and Traverse 3)
–	Rock positions	UTM 31 N position	258 positions (Traverse 1+2: 212 and Traverse 3: 46)

point along the *x*-axis pointing forward. The wheels are indexed starting from the front left, where odd numbers are used for the left side and even ones for the right (see Fig. 5). The four steering angles are indexed according to

Table 5. Overview of the file formats for all data collected. In stereo images, {0,1} corresponds to the left and right images respectively.

File Name	Description	Format
LocCam_YYYY_MM_DD_hh_mm_ss_fff_{0,1}	Color, 1024 × 768 raw stereo image pairs	
PanCam_YYYY_MM_DD_hh_mm_ss_fff_{0,1}	Color, 1280 × 960 raw stereo image pairs	
ToF_YYYY_MM_DD_hh_mm_ss_fff_{range, intensity}	16-bit grayscale, 176 × 144 raw images	
Velodyne_YYYY_MM_DD_hh_mm_ss_fff_{range, intensity}	16-bit grayscale, 1808 × 16 raw images (note: intensity images are 8-bit)	
gps-latlong.txt	GPS measurements of latitude, longitude and altitude expressed on WGS 84 ellipsoid	Timestamp, signal quality, latitude (°), longitude (°), altitude (m), latitude standard deviation (m), longitude standard deviation (m), altitude standard deviation (m)
gps-utm31.txt	GPS measurements in UTM 31 N coordinates	Timestamp, signal quality, northing (m), easting (m), altitude (m), northing standard deviation (m), easting standard deviation (m), altitude standard deviation (m)
imu.txt	Accelerometer, gyroscope and inclinometer measurements	Timestamp, x, y, z, acceleration (m/s^2), x, y, z, angular velocity (rad/s), x, y, z, acceleration (m/s^2)
odometry.txt	Wheel and steering angular displacement and rocker-bogie potentiometer measurements	Timestamp, front left, front right, center left, center right, back left, back right *wheel* angular displacement (rad), front left, front right, back left, back right *steering* angular displacement (rad), rocker, left bogie, right bogie orientation (rad)
ptu.txt	Pan–tilt unit orientation	Timestamp, pan (rad), tilt (rad)
{small, medium, large}-rocks-traverse{12,3}.txt	Artificial rock coordinates	Latitude (°), longitude (°)
{small, medium, large}-rock.{sldprt,step}	Artificial rock 3D models	.sldprt, .step
dsm.tif	Digital elevation model	.tif
mosaic.tif	Georeferenced image	.tif

the associated wheel index. The rocker and bogie orientations are indexed with 1 on the left side and 2 on the right, and the rocker orientations are equal and opposite (i.e. $\psi_2 = -\psi_1$). For the sake of brevity, the transformation between each wheel reference frame and the IMU reference frame is not displayed here, but can be generated as a 4 × 4 transformation matrix with the MAT-LAB® script (`wheelTransformation.m`). The wheel diameters (not including grousers) are 0.250 m, the wheel widths are 0.120 m, and the distance between the centers of adjacent wheels is 0.817 m.

The Velodyne and ToF camera data are stored as 16-bit grayscale images (except in the case of the 8-bit Velodyne intensity image). Storing this data in a structured way can be useful when computing nearest neighbor points, applying 2D feature-tracking algorithms, or for compression. To convert these to 3D point clouds, the Velodyne range images

should be multiplied by 1.0 mm to obtain the absolute range. The azimuth image should be divided by 100.0 to obtain the azimuth in degrees. Each of the 16 rows in the image corresponds to a specific elevation value in degrees that can be found in the VLP-16 manual. Similarly, the ToF range image, $\mathbf{\Phi}$, represents a percentage of the maximum range value (in this case the maximum grayscale integer value of 2^{14} corresponds to the maximum range, 9.993 m). Therefore, the absolute range image $\mathbf{D}$, in meters, can be calculated by

$$\mathbf{D} = \frac{9.993}{2^{14}}\mathbf{\Phi} \qquad (8)$$

By using the intrinsic parameters of the ToF camera included on the dataset website, a 3D point that corresponds to each range value can be computed. Alternatively a MAT-LAB® script (`image2points.m`) is provided that can convert any Velodyne range and azimuth image pair, ToF
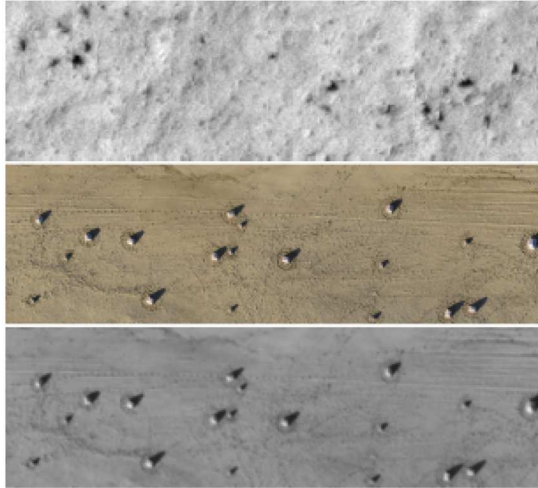
Fig. 6. Images covering an 80 m×20 m area. Top: HiRise imagery of rocks in Gale Crater, Mars. Middle: raw UAV imagery of artificial rocks. Bottom: processed UAV imagery of artificial rocks simulating the specifications of the HiRise camera.

range image, PanCam, or LocCam stereo image pairs to a 3D point cloud. Velodyne range and azimuth image pair, ToF range image, PanCam stereo image pair, or LocCam stereo image pair.

Table 1 summarizes the data collected over each traverse and Table 5 summarizes the file formats. Note that each traverse is partitioned into five-minute intervals to make downloading the dataset more manageable.

3. UAV flight data

The eBee UAV is a fixed-wing aircraft with a camera mounted to its belly. It also includes an integrated sensor suite with inertial sensors and a GPS receiver that are used to estimate its orientation and position. By imaging multiple overlapping areas, the eBee's proprietary software uses offline bundle adjustment to create a geotiff—a single image that covers the entire area of the traverse—where each pixel has a corresponding 2D position in the global UTM reference system, as well as a digital surface model image where each pixel provides an estimate of elevation according to the WGS 84 ellipsoid. This information is useful to researchers because it provides an analog to satellite imagery that exists on Mars and on Earth, and has shown promise for use in global localization in GNSS-denied environments (Boukas et al., 2015; Hourdakis and Lourakis, 2015) by matching regions of interest in satellite imagery to imagery obtained from the ground (Boukas and Gasteratos, 2016).

Because the source data is of a much higher resolution, it is possible to create simulated satellite imagery when knowing the resolution and the point spread function (PSF) of the satellite in question (Hlavka, 1986). In the case of the HiRise camera on-board MRO, the PSF is between one and

two pixels wide at full width half maximum, and the resolution is between 25 cm/pixel and 30 cm/pixel (McEwen et al., 2007). An example of this is shown in Fig. 6, where an image has been processed to replicate the satellite imagery available on Mars by convolving the high-resolution image with a Gaussian kernel that approximates the PSF, and then resizing the image using nearest-neighbor interpolation.

4. Discussion

This section provides some further discussion and "lessons learned" throughout and following the field campaign in which the presented data was collected and compiled.

In total, HDPR traversed 2.044 km in this field campaign; its mobility system, computer and all sensors were powered by a 1000 W, Honda EU10i generator. At a nominal speed of 0.6 m/s on flat, sandy terrain, HDPR draws approximately 550 W. The 450 W margin allows it to safely drive over undulating terrain and up slopes of at least 10°.

This level of performance on sandy terrain was needed as the mechanical properties of sand are similar to those of planetary soil and it is often used as a planetary soil simulant (Cross et al., 2013; Ding et al., 2009; Setterfield and Ellery, 2012). Having a dataset collected at a relatively fast speed is useful for testing algorithms meant for a future Sample Fetch Rover concept that will require much faster traverses than those conducted in past missions. It also enables long traverses to test the accuracy of localization algorithms.

The dataset provided is representative of the ExoMars rover due to its similar sensor suite while also including modern 3D LiDAR sensors that have not been used on a rover mission to date. This has allowed comparison between the two sets of sensors to evaluate their relative advantages and disadvantages. For instance, the lighting conditions are particularly challenging for visual odometry algorithms in Traverse 2, whereas this has little affect on the LiDAR data.

The provided `image2points.m` function can be used to generate 3D point clouds in the camera frame. These can be used for digital elevation map generation or in visual odometry. The output of this function is an $m \times n \times k$ matrix where m and n are the height and width of the image in pixels and k is the length of the vector representing a single point. Velodyne and ToF matrices contain 3D position and intensity whereas LocCam and PanCam matrices contain 3D position and red-green-blue (RGB) color. This preserves the order of the data in the image space, making it easy to perform many related tasks (e.g. surface normal extraction, 2D feature correspondence, interpolation, etc.).

The data has also helped the team identify areas for improvement in preparing for future field campaigns. For example, the utilized IMU was selected for its high-accuracy gyroscope and accelerometer, but it did not include a magnetometer. This is similar to the ExoMars rover (on Mars there is no global magnetic field to measure). However, the addition of a magnetometer (on Earth)

would serve to provide better ground truth for the rover's heading than one derived solely from GPS measurements. Wi-Fi was utilized for communication between a base station located at the beginning of the traverse and the rover, allowing images from the rover to be displayed over the high-bandwidth connection in real time for use in operations. However, Wi-Fi connectivity issues caused missed RTK updates, resulting in small parts of the traverse that have a less accurate ground-truth GPS measurement. The signal quality is label led in the dataset as either *RTK_FIXED*, *RTK_FLOAT*, or *DIFFERENTIAL* and their respective accuracies are reflected in each measurement's recorded standard deviation. This has been improved for future tests by extending the Wi-Fi network across the traverse area to reduce dropouts.

5. Summary

This paper presents a time-registered multi-sensor rover traverse dataset captured in a unique outdoor Mars-analog environment, along with georeferenced high-resolution imagery of the traversed terrain. This dataset will be useful to the robotics research community, particularly those interested in navigation in GNSS-denied environments, as in the case of planetary rovers. The data can be used to test algorithms that aim to combine various forms of perception. Because three of the sensors were mounted together such that much of their field of view overlapped, comparisons (for instance, running visual odometry algorithms) between the different sensors is facilitated.

References

Bakambu J, Langley C, Pushpanathan G, et al. (2014) Field trial results of planetary rover visual motion estimation in Mars analogue terrain. *Journal of Field Robotics* 29(3): 413–425.

Bakambu JN, Langley C, Leineweber KC, et al. (2016) Maturing Canadian autonomous guidance, navigation, and control of planetary rovers. In: *International symposium on artificial intelligence, robotics and automation in space, i-SAIRAS international executive committee*, Beijing, China. 19–22 June 2016. Noordwijk, The Netherlands: European Space Agency. Available at: https://robotics.estec.esa.int/i-SAIRAS/isairas2016/Session4c/S-4c-1-ChristopherLangley.pdf

Boukas E and Gasteratos A (2016) Modeling regions of interest on orbital and rover imagery for planetary exploration missions. *Cybernetics and Systems* 47(3): 180–205.

Boukas E, Gasteratos A and Visentin G (2015) Towards orbital based global rover localization. In: *IEEE international conference on robotics and automation (ICRA)*, Seattle, WA, 26–30 May 2015, pp. 2874–2881. Washington, DC: IEEE.

Boukas E, Hewitt RA, Pagnamenta M, et al. (2016) HDPR: A mobile testbed for current and future rover technologies. In: *International symposium on artificial intelligence, robotics and automation in space, i-SAIRAS international executive committee*, Beijing, China. 19–22 June 2016. Noordwijk, The Netherlands: European Space Agency. Available at: https://robotics.estec.esa.int/i-SAIRAS/isairas2016/Session4c/S-4c-1-ChristopherLangley.pdf

Coates AJ, Jaumann R, Schmitz N, et al. (2015) PanCam on the ExoMars 2018 Rover: A stereo, multispectral and high-resolution camera system to investigate the surface of Mars. In: *Lunar and planetary science conference*, The Woodlands, Texas, USA, 16–20 March 2015, vol. 46, pp. 1812–1813. Houstan, Texas, USA: Lunar and Planetary Institute.

Cross M, Ellery A and Qadi A (2013) Estimating terrain parameters for a rigid wheeled rover using neural networks. *Journal of Terramechanics* 50: 165–174.

Ding L, Yoshida K, Nagatani K, et al. (2009) Parameter identification for planetary soil based on a decoupled analytical wheel-soil interaction terramechanics model. In: *IEEE/RSJ international conference on intelligent robots and systems (IROS)*, St. Louis, MO, 10–15 October 2009, pp. 4122–4127. Washington, DC: IEEE.

Furgale PT, Carle P, Enright J, et al. (2012) The Devon Island rover navigation dataset. *The International Journal of Robotics Research* 31(6): 707–713.

Golombek M, Huertas A, Kipp D, et al. (2012) Detection and characterization of rocks and rock size-frequency distributions at the final four Mars Science Laboratory landing sites. *International Journal of Mars Science and Exploration* 7: 1–22.

Hewitt RA and Marshall JA (2015) Towards intensity-augmented SLAM with LiDAR and ToF sensors. In: *IEEE/RSJ international conference on intelligent robots and systems (IROS)*, Hamburg, Germany, 28 September–2 October 2015, pp. 1956–1961. Washington, DC: IEEE.

Hlavka CA (1986) *Simulation of LANDSAT multispectral scanner spatial resolution with airborne scanner data*. Technical Report NASA-TM-86832, NASA Ames Research Center, Moffett Field, CA.

Hourdakis E and Lourakis M (2015) Countering drift in visual odometry for planetary rovers by registering boulders in ground and orbital images. In: *IEEE/RSJ international conference on intelligent robots and systems (IROS)*, Hamburg, Germany, 28 September–2 October 2015, pp. 111–116. Washington, DC: IEEE.

McEwen AS, Eliason EM, Bergstrom JW, et al. (2007) Mars Reconnaissance Orbiter's high resolution imaging science experiment (HiRise). *Journal of Geophysical Research: Planets* 112: 1991–2012.

McManus C, Furgale PT and Barfoot TD (2013) Lighting-invariant visual teach and repeat using appearance-based Lidar. *Journal of Field Robotics* 30(2): 254–287.

Setterfield T and Ellery A (2012) Terrain response estimation using an instrumented rocker-bogie mobility system. *IEEE Transactions on Robotics* 29: 172–188.

Wettergreen D, Tompkins P, Urmson C, et al. (2005) Sun-synchronous robotic exploration: Technical description and field experimentation. *The International Journal of Robotics Research* 24(1): 3–30.

Woods M, Shaw A, Tidey E, et al. (2014a) Seeker – autonomous long-range rover navigation for remote exploration. *Journal of Field Robotics* 31(6): 940–968.

Woods M, Shaw A, Wallace I, et al. (2014b) Demonstrating autonomous Mars rover science operations in the Atacama Desert. In: *International symposium on artificial intelligence, robotics and automation in space, i-SAIRAS international executive committee*, Montreal, Canada. 17–19 June 2014. Noordwijk, The Netherlands: European Space Agency. Available at: https://robotics.estec.esa.int/i-SAIRAS/isairas2014/Data/Session%205a/ISAIRAS_FinalPaper_0019.pdf